

## PROBING THE FERMI BUBBLES IN ULTRAVIOLET ABSORPTION: A SPECTROSCOPIC SIGNATURE OF THE MILKY WAY'S BICONICAL NUCLEAR OUTFLOW<sup>1</sup>

ANDREW J. FOX<sup>2</sup>, RONGMON BORDOLOI<sup>2</sup>, BLAIR D. SAVAGE<sup>3</sup>, FELIX J. LOCKMAN<sup>4</sup>, EDWARD B. JENKINS<sup>5</sup>, BART P. WAKKER<sup>3</sup>, JOSS BLAND-HAWTHORN<sup>6</sup>, SVEA HERNANDEZ<sup>2</sup>, TAE-SUN KIM<sup>7</sup>, ROBERT A. BENJAMIN<sup>8</sup>, DAVID V. BOWEN<sup>5</sup>, & JASON TUMLINSON<sup>2</sup>

<sup>2</sup> Space Telescope Science Institute, 3700 San Martin Drive, Baltimore, MD 21218

<sup>3</sup> Department of Astronomy, University of Wisconsin–Madison, 475 North Charter St., Madison, WI 53706

<sup>4</sup> National Radio Astronomy Observatory, P.O. Box 2, Rt. 28/92, Green Bank, WV 24944

<sup>5</sup> Princeton University Observatory, Princeton, NJ 08544

<sup>6</sup> Institute of Astronomy, School of Physics, University of Sydney, NSW 2006, Australia

<sup>7</sup> Osservatorio Astronomico di Trieste, Via G.B. Tiepolo 11, 34143 Trieste, Italy

<sup>8</sup> Department of Physics, University of Wisconsin–Whitewater, 800 W. Main St., Whitewater, WI 53190

*Draft version November 5, 2018*

### ABSTRACT

Giant lobes of plasma extend  $\approx 55^\circ$  above and below the Galactic Center, glowing in emission from gamma rays (the Fermi Bubbles) to microwaves (the WMAP haze) and polarized radio waves. We use ultraviolet absorption-line spectra from the *Hubble Space Telescope* to constrain the velocity of the outflowing gas within these regions, targeting the quasar PDS 456 ( $\ell, b = 10.4^\circ, +11.2^\circ$ ). This sightline passes through a clear biconical structure seen in hard X-ray and gamma-ray emission near the base of the northern Fermi Bubble. We report two high-velocity metal absorption components, at  $v_{\text{LSR}} = -235$  and  $+250 \text{ km s}^{-1}$ , which cannot be explained by co-rotating gas in the Galactic disk or halo. Their velocities are suggestive of an origin on the front and back side of an expanding biconical outflow emanating from the Galactic Center. We develop simple kinematic biconical outflow models that can explain the observed profiles with an outflow velocity of  $\gtrsim 900 \text{ km s}^{-1}$  and a full opening angle of  $\approx 110^\circ$  (matching the X-ray bicone). This indicates Galactic Center activity over the last  $\approx 2.5\text{--}4.0 \text{ Myr}$ , in line with age estimates of the Fermi Bubbles. The observations illustrate the use of UV spectroscopy to probe the properties of swept-up gas venting into the Fermi Bubbles.

*Subject headings:* Galaxy: center — Galaxy: halo — Galaxy: evolution — ISM: jets and outflows — ISM: kinematics and dynamics

### 1. INTRODUCTION

The nuclei of star-forming galaxies are the powerhouses where super-massive black holes collect interstellar gas from their surroundings, funnel it onto accretion disks, and heat it to extreme temperatures. The energy released from these environments and from supernovae drives gas out of galaxies through large-scale Galactic winds (see reviews by Heckman 2002; Veilleux et al. 2005). Many outflows in nearby star-forming galaxies are nuclear in origin and biconical in shape, as in NGC 3079 (Cecil et al. 2001, 2002), M82 (Bland & Tully 1988; Shopbell & Bland-Hawthorn 1998; Ohyama et al. 2002), and NGC 1482 (Veilleux & Rupke 2002).

Our vantage point inside the dusty rotating disk of the Milky Way hampers our knowledge of any *Galactic* nuclear outflow. Lockman (1984) noted an absence of H I in the inner Galaxy and suggested it had been cleared out by a wind. The first clear detection of a biconical outflow was made in mid-IR emission and (on larger scales) in hard X-ray emis-

sion (Bland-Hawthorn & Cohen 2003). It has since become clear that the Galactic Center (GC) lies between two giant, energetic lobes associated with outflowing gas. These lobes extend  $\approx 55^\circ$  above and below the GC ( $\approx 12 \text{ kpc}$ ) and show enhanced emission across the electromagnetic spectrum, including: (1)  $\gamma$ -ray emission, i.e. the Fermi Bubbles (FBs; Su et al. 2010; Dobler et al. 2010; Ackermann et al. 2014); (2) soft X-ray emission (0.3–1.0 keV; Snowden et al. 1997; Kataoka et al. 2013); (3) K-band microwave emission (23–94 GHz), known as the so-called WMAP haze (Finkbeiner et al. 2004; Dobler & Finkbeiner 2008); (4) polarized radio emission at 2.3 GHz (synchrotron radiation; Carretti et al. 2013). Near the base of the FBs, within 700 pc of the GC, McClure-Griffiths et al. (2013, hereafter MG13) recently discovered a population of  $\approx 100$  small H I clouds whose kinematics are consistent with a biconical outflow with a velocity of  $\approx 200 \text{ km s}^{-1}$ .

Clearly, a nuclear outflow is being driven out from the GC. Yet only a handful of GC sightlines have published UV spectroscopy that constrains the kinematics, ionization state, and elemental abundances of the nuclear outflow, including two AGN directions (Keeney et al. 2006) and several stellar directions (Bowen et al. 2008; Zech et al. 2008; Wakker et al. 2012). However, none of these UV studies have probed a full sightline through the front and back sides of the FBs within  $20^\circ$  of the GC, where the  $\gamma$ -ray emission, X-ray emission, and (presum-

afox@stsci.edu

<sup>1</sup> Based on observations taken under program 13448 of the NASA/ESA Hubble Space Telescope, obtained at the Space Telescope Science Institute, which is operated by the Association of Universities for Research in Astronomy, Inc., under NASA contract NAS 5-26555, and under program 14B-299 of the NRAO Green Bank Telescope, which is a facility of the National Science Foundation operated under cooperative agreement by Associated Universities, Inc.

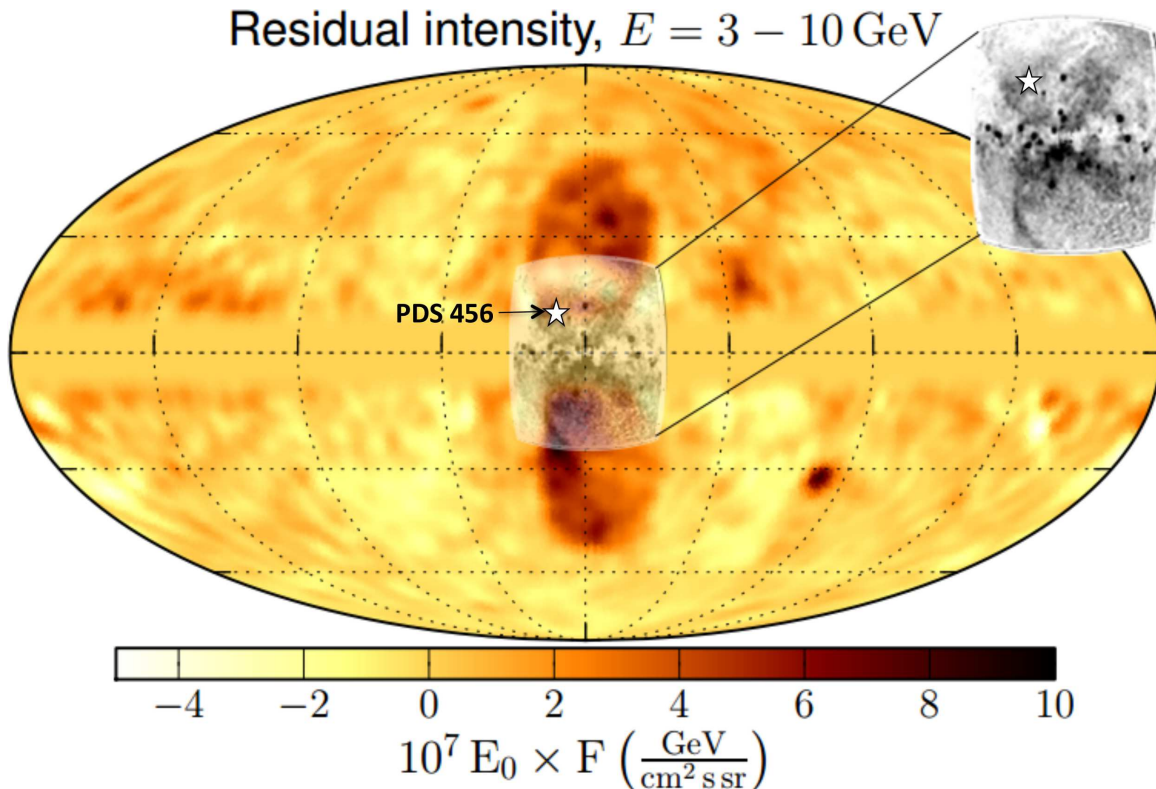


FIG. 1.— Collage of gamma-ray and X-ray emission showing the striking biconical nuclear structure intercepted by the PDS 456 sightline. The yellow/orange map is an all-sky *Fermi* image of the residual gamma-ray intensity in the 3–10 GeV range, in Galactic coordinates centered on the GC (Ackermann et al. 2014; © AAS. Reproduced with permission). The Fermi Bubbles are the twin lobes in dark orange at the center of the figure. Superimposed in gray-scale is the *ROSAT* diffuse 1.5 keV emission map, based on Snowden et al. 1997, Bland-Hawthorn & Cohen 2003, and Veilleux et al. 2005. The inset on the right shows a zoom-in on the X-ray data. Adapted from Figure 22, *The Spectrum and Morphology of the Fermi Bubbles*, M. Ackermann et al., *ApJ*, Volume 793, Issue 1, 2014, Page 64.

ably) wind activity is strongest. The only such sightline with published data is the *optical* spectrum of the blue supergiant LS 4825 ( $l, b = 1.7^\circ, -6.6^\circ$ ,  $d = 21 \pm 5$  kpc), which shows complex multi-component Ca II and Na I profiles spanning  $\approx 300$  km s $^{-1}$  (Ryans et al. 1997).

We have initiated an observing program with the *Hubble Space Telescope* (*HST*) to study the gas in the GC region (defined here as  $0^\circ < l < 30^\circ$  and  $330^\circ < l < 360^\circ$ ) with UV spectroscopy (Program IDs 12936 and 13448). The quasar PDS 456 ( $z_{em} = 0.184$ ,  $l, b = 10.4^\circ, +11.2^\circ$ , also known as IRAS 17254-1413) is the lowest latitude and smallest impact parameter to the GC ( $\rho = 2.3$  kpc) of any AGN in our sample. Furthermore, this sightline is *the only AGN direction in our sample that passes through the biconical region of enhanced ROSAT 1.5 keV X-ray emission* centered on the GC (Snowden et al. 1997), where the  $\gamma$ -ray emission is also strong since the direction intersects the base of the northern FB (Su et al. 2010). The PDS 456 direction (see Figure 1) is therefore of high interest for looking for UV outflow signatures. There are no known 21 cm (neutral) high-velocity clouds (HVCs) in this direction (e.g. Putman et al. 2012).

In this Letter we present new UV and radio spectra of PDS 456 to explore the properties of gas entrained in the Galactic nuclear outflow. In Section 2 we discuss the observations and their reduction. In Section 3 we present the UV absorption-line spectra and discuss the identification of outflow components. Motivated by the component structure observed in our spectra, we present numerical kinematic models of a nuclear biconical out-

flow in Section 4. In Section 5 we present a discussion of our results. A full discussion of other directions that penetrate the northern and southern FBs will be presented in an upcoming paper.

## 2. OBSERVATIONS AND DATA REDUCTION

### 2.1. COS Spectra

PDS 456 was observed on February 10 2014 with the Cosmic Origins Spectrograph (COS; Green et al. 2012) onboard *HST* for a total of five orbits. The observations used the G130M/1291 and G160M/1600 grating/central wavelength settings, all four FP-POS positions, and exposure times of 4846 s for G130M and 8664 s for G160M. Individual exposures were aligned in velocity space using the centroids of known low-ion interstellar absorption lines, and then co-added following the same procedures as described in Fox et al. (2014). The spectra have a velocity resolution (FWHM) of  $\approx 20$  km s $^{-1}$ , a signal-to-noise ratio near the absorption lines of interest of  $\approx 12$ –20 (per resolution element), an absolute velocity scale uncertainty of  $\approx 5$  km s $^{-1}$ , and cover the wavelength interval 1133–1778 Å, with small gaps between detector segments at 1279–1288 and 1587–1598 Å. The spectra were normalized around each absorption line using linear continua and for display are rebinned by seven pixels (one resolution element), though the Voigt-profile fits (described below) were made on the unbinned data.

### 2.2. GBT Spectra

We obtained several deep H I 21 cm pointings of the PDS 456 direction using the Green Bank Telescope (GBT) under NRAO program GBT/14B-299, with the goal of detecting the HV components in emission. Multiple scans of PDS 456 were taken on October 3 and October 4 2014 with the VEGAS spectrometer in frequency-switching mode, for a total of 35 minutes of integration. The data were taken by frequency-switching either 3.6 or 4.0 MHz, resulting in an unconfused velocity range of at least  $760 \text{ km s}^{-1}$  about zero velocity at an intrinsic channel spacing of  $0.151 \text{ km s}^{-1}$ . The spectra were Hanning smoothed, then calibrated and corrected for stray radiation using the procedure described by Boothroyd et al. (2011). One of the receiver's two linear polarizations (PLNUM=1) gave consistently superior instrumental baselines so only those data were used. A fourth-order polynomial was removed from emission-free portions of the final average. The resulting spectrum has an rms brightness temperature noise of  $17.5 \text{ mK}$  in a  $0.30 \text{ km s}^{-1}$  channel, giving a  $1\sigma$  sensitivity to a line  $40 \text{ km s}^{-1}$  wide (chosen to be typical of Galactic HVCs) of  $N(\text{H I})=1.1 \times 10^{17} \text{ cm}^{-2}$ .

### 3. IDENTIFICATION OF OUTFLOW COMPONENTS

The COS spectra of PDS 456 show four absorption components (see Figure 2), centered at  $v_{\text{LSR}}=-235, -5, +130,$  and  $+250 \text{ km s}^{-1}$ . Absorption is seen in low-ionization (C II, Si II, Al II), intermediate-ionization (Si III), and high-ionization (C IV, Si IV, N V) species, though the relative strength of absorption differs between components. The  $-235, -5,$  and  $+130 \text{ km s}^{-1}$  components show absorption in the low, intermediate, and high ions, whereas the  $+250 \text{ km s}^{-1}$  component is seen in the low- and intermediate ions only (no C IV, Si IV, or N V). H I emission in the GBT spectrum is only seen in the  $-5 \text{ km s}^{-1}$  component; in the other three components no H I detection is made down to a sensitive  $3\sigma$  upper limit  $N(\text{H I}) < 3.3 \times 10^{17} \text{ cm}^{-2}$ . The ionic column densities in the absorption components are given in Table 1. These were determined by fitting Voigt profiles to the data with the VPFIT software<sup>2</sup>, using simultaneous fits to all available lines of a given ion.

Foreground gas in the rotating disk of the Galaxy produces absorption at a range of LSR velocities, and a simple model of Galactic rotation can be used to predict the maximal allowed velocities for a given latitude and longitude (e.g. Savage & Massa 1987), assuming cylindrical co-rotation. Absorption detected *outside* this velocity interval can be attributed to inflow or outflow. Toward PDS 456 the minimum and maximum LSR velocities are  $\approx 0 \text{ km s}^{-1}$  (at a distance of 0.0 kpc) and  $+174 \text{ km s}^{-1}$  (at 8.8 kpc), respectively. Therefore:

- (1) the strong  $-5 \text{ km s}^{-1}$  component centered can be (either partially or completely) explained by foreground gas in the Galactic disk.
- (2) the  $+130 \text{ km s}^{-1}$  component corresponds to distances of 7.1 and 9.9 kpc for co-rotation and so could also be tracing Galactic material at  $z$ -distances of 1.4 and 1.9 kpc, respectively. However, for distant inner Galaxy sightlines, the assumption of co-rotation breaks down at  $|z| > 1 \text{ kpc}$  (Savage et al. 1990; Sembach et al. 1991), potentially because the gas has been cleared out by a wind.

<sup>2</sup> Available at <http://www.ast.cam.ac.uk/~rfc/vpfit.html>

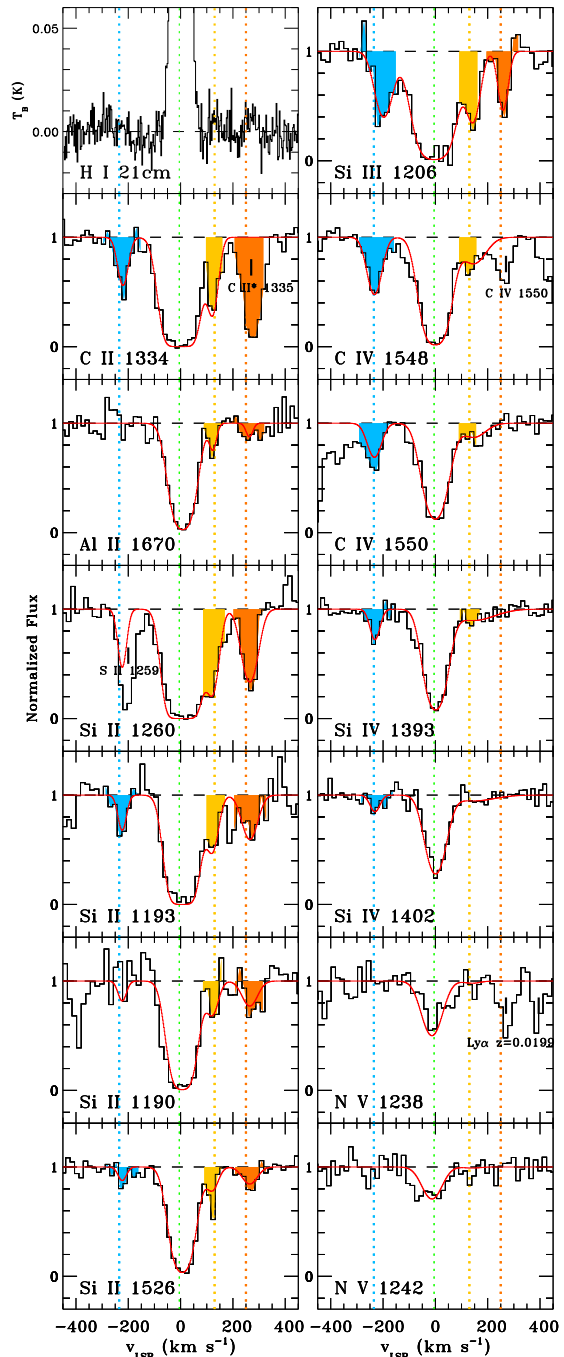


FIG. 2.— *HST*/*COS* and GBT spectra of the quasar PDS 456. Normalized flux is plotted against LSR velocity for all UV metal absorption lines that show high-velocity (HV) absorption (with low ions in the left column and intermediate/high ions in the right column). The GBT H I 21 cm emission spectrum is included in the top-left panel. Absorption-line components are observed at  $v_{\text{LSR}}=-235, -5, +130,$  and  $+250 \text{ km s}^{-1}$ ; only the  $-5 \text{ km s}^{-1}$  component is seen in 21 cm emission. Red lines indicate Voigt-profile fits. The  $-5 \text{ km s}^{-1}$  (unshaded) and  $+130 \text{ km s}^{-1}$  (yellow) components have velocities consistent with co-rotating foreground gas. However, the  $-235 \text{ km s}^{-1}$  (blue) and  $+250 \text{ km s}^{-1}$  (orange) components cannot be explained by co-rotation; instead, their velocities are suggestive of gas swept up by a biconical outflow. In this scenario the near-side of the outflowing cone gives the  $-235 \text{ km s}^{-1}$  component and the far-side gives the  $+250 \text{ km s}^{-1}$  component.

Thus the  $+130 \text{ km s}^{-1}$  component might trace a nuclear

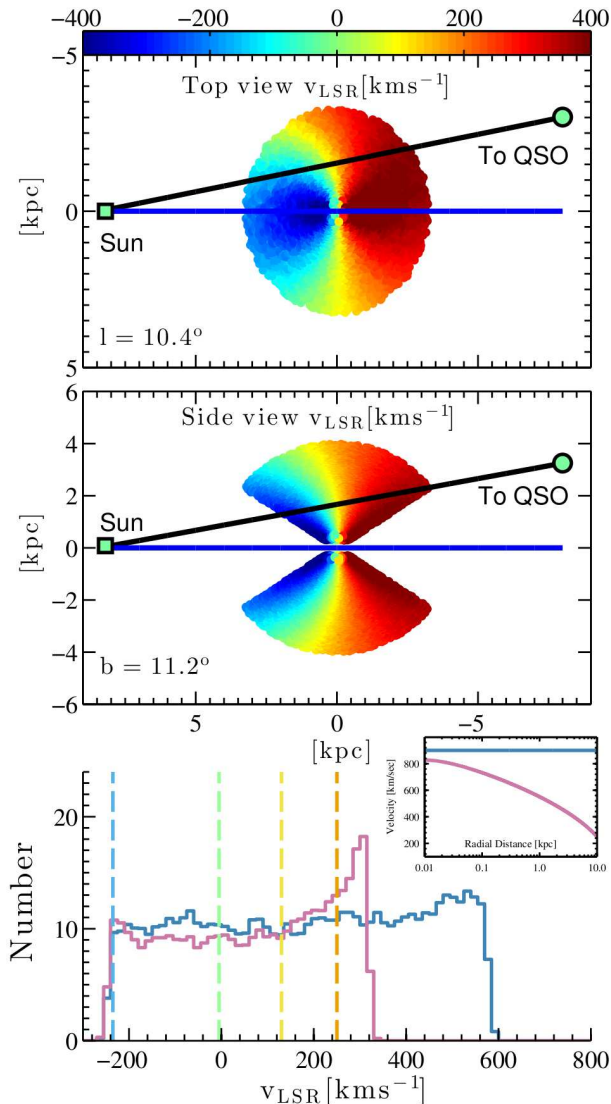


FIG. 3.— Numerical models of the Galactic biconical nuclear outflow, which can explain the observed absorption-line kinematics. The models have a constant outflow velocity of  $900 \text{ km s}^{-1}$  and a full opening angle of  $110^\circ$  (tuned to match the X-ray bicone). We investigate two sets of models: constant-velocity and momentum-driven. **Top:** Top view of the momentum-driven outflow, looking down on the Galactic plane. Each outflow particle is color-coded by its LSR velocity. The near side of the outflow is blueshifted and the far-side of the outflow is redshifted. **Middle:** Side view of the momentum-driven outflow, showing the latitude where the PDS 456 sightline intercepts the bicone. **Bottom:** Distribution of LSR velocities of the outflow particles along the PDS 456 sightline in 100 realizations of the models, for both the constant-velocity (blue line) and momentum-driven (purple line) cases. The inset panel shows the velocity profile of the two models. The centroids of the observed components in the PDS 456 spectrum are shown with vertical lines.

outflow, but we cannot conclusively determine its origin. (3) the  $-235$  and  $+250 \text{ km s}^{-1}$  components are at least  $235$  and  $76 \text{ km s}^{-1}$  away from co-rotation, respectively, and are therefore of most interest for a nuclear outflow. In the Galactic Standard of Rest (GSR), their velocities are  $-190$  and  $+295 \text{ km s}^{-1}$ , assuming the rotation velocity at the solar circle is  $+254 \text{ km s}^{-1}$  (Reid et al. 2009), and where  $v_{\text{GSR}} = v_{\text{LSR}} + 254 \sin \ell \cos b$ . The velocities of these two components are consistent with an origin on

the front (approaching) and back (receding) sides of a biconical nuclear outflow emanating from the GC, a scenario modeled in Section 4 and discussed in Section 5.

We note that the observed low-velocity high-ion absorption (C IV, Si IV, and N V) is strong compared to other (non-GC) Galactic halo sight lines (Savage et al. 2001; Wakker et al. 2012). In particular, C IV shows a  $\approx 0.5$  dex excess in low-velocity column density, which may be another sign of GC activity.

#### 4. BICONICAL OUTFLOW NUMERICAL MODELS

We develop simple numerical models to explore the kinematic predictions of a biconical nuclear outflow. The models are based on the Mg II outflow models of Bordoloi et al. (2014). We assume the outflow is a non-rotating expanding bicone centered on the GC with a constant mass flux. A population of  $10^7$  test particles is inserted at the base of the outflow, with a uniform filling factor. The three principal free parameters in the models are the initial outflow velocity  $v_{\text{out}}$ , the full opening angle  $\alpha$  of the bicone, and the velocity profile. We take  $\alpha = 110^\circ$  based on the bicone seen in the *ROSAT* 1.5 keV image (Figure 1) and investigate the value of  $v_{\text{out}}$  needed to explain the  $-235$  and  $+250 \text{ km s}^{-1}$  components. We explore two cases for the velocity profile: constant-velocity (the simplest case), and momentum-driven, where the outflow climbs ballistically out of the Galactic potential after being given an initial impulse (e.g. by ram pressure from a hot wind). In the latter case we use the formalism of Murray et al. (2005) and Dijkstra & Kramer (2012) to express the velocity as a function of radius from the GC. We assume the outflow reaches a radial distance of at least 4 kpc, distant enough to ensure the PDS 456 sightline fully intercepts the bicone (see Figure 3, middle panel). The models are initially computed in the GSR reference frame, but are transformed into the LSR frame for comparison with the data. For both the constant-velocity and momentum-driven cases, 100 realizations of the models are created, and for each one a line-of-sight with the PDS 456 coordinates was generated and the kinematic structure measured. The models do not account for the physical or kinematic properties of the external gaseous medium that confines the flow.

The models are shown in Figure 3. We find  $v_{\text{out}} \gtrsim 900 \text{ km s}^{-1}$ ; lower velocities do not account for the  $-235 \text{ km s}^{-1}$  component. Figures 3a (top view) and 3b (side view) show the velocity structure of the outflow as observed from vantage points outside the Galaxy. These plots illustrate the correspondence between LSR velocity and distance along the line-of-sight. The velocity fields are asymmetric with respect to the vertical because of the transformation from the GSR to LSR frame, i.e. because we are observing the outflow from a co-rotating frame at a fixed distance. Figure 3c shows the distribution of outflow velocities projected onto the PDS 456 line-of-sight drawn from 100 realizations of each of the two models. Discrete kinematic structure is seen in any single realization of the model (not shown in figure), but the component velocities differ substantially between any two model runs, so we show the distribution to indicate the *range* of velocities predicted.

There are several points to note from the model velocity distributions. First, the distributions are fairly flat for both constant-velocity and momentum-driven winds,

which reflects our choice of model in which gas exists with uniform filling factor within the outflow, not just at the edges. The prediction of outflowing gas with LSR velocities near  $0 \text{ km s}^{-1}$  could explain the 0.5 dex excess in low-velocity high-ion absorption seen toward PDS 456. Second, the distributions are *asymmetric* around zero, ranging from  $\approx -250 \text{ km s}^{-1}$  (this velocity is a consequence of the requirement that we explain the  $-235 \text{ km s}^{-1}$  component toward PDS 456) to  $\approx +550 \text{ km s}^{-1}$  for the constant-velocity wind, and  $\approx +300 \text{ km s}^{-1}$  for the momentum-driven wind. This asymmetry is a projection effect arising because of the finite distance between the Sun and the GC (the near-field effect). Third, the momentum-driven wind model is more successful in reproducing the range of velocity components seen toward PDS 456 than the constant-velocity wind model, since the latter predicts gas in the range  $\approx 300\text{--}600 \text{ km s}^{-1}$ , which is not observed. Models in which gas flows out preferentially along the edges of the cone are also consistent with the data, but are outside the scope of this Letter. In summary, the simple momentum-driven biconical wind model is able to reproduce the velocities of the HV components toward PDS 456.

## 5. DISCUSSION

The *HST*/COS spectrum of PDS 456, a QSO lying only  $15.2^\circ$  from the GC in a direction of enhanced X-ray and  $\gamma$ -ray emission intercepting the base of the northern FB, shows UV metal-absorption-line components at  $v_{\text{LSR}} = -235$  and  $+250 \text{ km s}^{-1}$  (corresponding to  $v_{\text{GSR}} = -190$  and  $+295 \text{ km s}^{-1}$ ), velocities which cannot be explained by gas in the low halo of the inner Galaxy co-rotating with the disk. A further component at  $+130 \text{ km s}^{-1}$  is also difficult to explain via co-rotation. None of the components shows 21 cm emission in our GBT spectrum down to sensitive levels of  $N(\text{H I}) < 3.3 \times 10^{17} \text{ cm}^{-2}$  ( $3\sigma$ ), which indicates the hydrogen is mostly ionized. The kinematics of these components can be explained in a scenario where cool swept-up gas is entrained on the near- (blueshifted) and far- (redshifted) side of a biconical outflow from the GC.

There are several arguments supporting the biconical outflow explanation: (1) the *ROSAT* X-ray imaging and *Fermi*  $\gamma$ -ray imaging both clearly indicate the presence of a biconical structure centered on the GC and intersected by the PDS 456 sightline; (2) simple kinematic models of a biconical outflow (Section 4) naturally reproduce the presence of both negative- and positive-velocity gas components; (3) such models also explain the excess low-velocity high-ion absorption; (4) the MG13 results demonstrate a population of H I clumps existing closer to the GC with kinematics consistent with a biconical outflow; (5) although we cannot rule out the possibility that individual HV absorbers arise in unrelated foreground or background HVCs, which have a sky covering fraction in UV metal lines of  $\approx 68\text{--}80\%$  (Collins et al. 2009; Shull et al. 2009; Lehner et al. 2012), a *chance alignment* of two unrelated HVCs at close-to-symmetric velocities of  $-235$  and  $+250 \text{ km s}^{-1}$  would be needed to emulate the profiles of a biconical outflow; (6) given the low latitude of the PDS 456 sightline ( $b = +11.2^\circ$ ), explaining the  $-235$  and  $+250 \text{ km s}^{-1}$  components as being regular (non-GC)

HVCs would require unusually large ( $\gtrsim 1000 \text{ km s}^{-1}$ ) vertical inflow or outflow velocities, because of the projection factor  $\sin b$ . This makes it highly unlikely that the PDS 456 HV components are due to regular HVCs or to tidally-stripped material like the Magellanic Stream, which have much lower vertical flow velocities ( $\sim 100\text{--}200 \text{ km s}^{-1}$ ).

In the biconical outflow interpretation, the hot wind phase is feeding the FBs with new plasma (e.g. Crocker 2012), whereas the cool low-ion gas represents swept-up material entrained in the outflow. We stress that our *HST*/COS observations do not directly probe the hot phase, but instead probe cool ( $T \sim 10^4 \text{ K}$ ) entrained gas via the low ions and transition-temperature ( $T \sim 10^5 \text{ K}$ ) gas via the high ions, which may trace the boundaries between the cool gas and the hot wind. The cool outflowing gas has already been detected, albeit closer to the GC with a much lower wind velocity, via the MG13 population of H I clouds. Despite the disruptive instabilities that can destroy cold filaments and clouds on short timescales, simulations show that such structures can survive in the hot wind fluid if stabilized by magnetic fields or other mechanisms (Cooper et al. 2008; McCourt et al. 2014).

Our models find the outflow velocity is  $\gtrsim 900 \text{ km s}^{-1}$ ; such a flow must be  $\approx 2.5\text{--}4.0 \text{ Myr}$  old to reach 2.3 kpc, the impact parameter of the PDS 456 sightline. This wind age is consistent with the timescale of energy injection that created the FBs, whether via AGN jets (Guo & Mathews 2012; Yang et al. 2012), feedback from nuclear star formation (Crocker & Aharonian 2011; Carretti et al. 2013; Lacki 2014), accretion flows onto Sgr A\* (Cheng et al. 2011; Mou et al. 2014), or a spherical outflow from Sgr A\* (Zubovas et al. 2011). It is also compatible with the observed H $\alpha$  emission from the Magellanic Stream, which is consistent with an origin following a Seyfert flare at the GC 1–3 Myr ago (Bland-Hawthorn et al. 2013).

In our upcoming work, we will analyze the UV spectra of other GC targets, including foreground stars at a range of distance and background AGN at a range of latitude, both inside and outside the FBs. A large sample of sightlines is needed to fully characterize the extent and nature of the Galactic nuclear outflow.

*Acknowledgments.* Support for program 13448 was provided by NASA through grants from the Space Telescope Science Institute, which is operated by the Association of Universities for Research in Astronomy, Inc., under NASA contract NAS 5-26555. The National Radio Astronomy Observatory is a facility of the National Science Foundation operated under cooperative agreement by Associated Universities, Inc. We thank Gerald Cecil for assistance with Figure 1 and the referee for an insightful report. We thank Anne Franckowiak and the Fermi-LAT collaboration for permission to reproduce their all-sky residual intensity map. JBH is funded by an ARC Laureate Fellowship. TSK acknowledges support from a European Research Council Starting Grant in cosmology and the IGM under Grant Agreement (GA) 257670.

TABLE 1  
COLUMN DENSITIES IN THE METAL ABSORPTION COMPONENTS TOWARD PDS 456<sup>a</sup>

$v_{\text{LSR}}$ ( $\text{km s}^{-1}$ )	$\log N(\text{Si II})$	$\log N(\text{Si III})$	$\log N(\text{Si IV})$	$\log N(\text{C II})$	$\log N(\text{C IV})$	$\log N(\text{N V})$	$\log \frac{N(\text{C IV})}{N(\text{Si IV})}$
-235	13.02±0.08	13.13±0.05	12.90±0.06	13.80±0.14	13.79±0.05	...	0.89±0.07
-5 <sup>b</sup>	14.76±0.05	>14.04	14.05±0.05	...	14.71±0.05	14.09±0.05	0.66±0.05
+130 <sup>b</sup>	13.40±0.05	13.06±0.05	13.03±0.16	14.14±0.12	13.58±0.06	...	0.28±0.17
+250	13.37±0.05	12.85±0.05	...	...	...	...	...

<sup>a</sup> Errors are statistical only. No entry is given for blends, non-detections, or heavily saturated lines.

<sup>b</sup> Velocity compatible with either a rotating disk or a nuclear outflow.

#### REFERENCES

- Ackermann, M., Albert, A., Atwood, W., et al. 2014, *ApJ*, 793, 64  
Bland, J. & Tully, B. 1988, *Nature*, 334, 43  
Bland-Hawthorn, J. & Cohen, M. 2003, *ApJ*, 582, 246  
Bland-Hawthorn, J., et al. 2013, *ApJ*, 778, 58  
Boothroyd, A. I, et al. 2011, *A&A*, 536, A81  
Bordoloi, R., et al. 2014, *ApJ*, 784, 108  
Bowen, D. V., et al. 2008, *ApJS*, 176, 59  
Carretti, E., et al. 2013, *Nature*, 493, 66  
Cecil, G., et al. 2001, *ApJ*, 555, 338  
Cecil, G., Bland-Hawthorn, J., & Veilleux, S., 2002, *ApJ*, 576, 745  
Cheng, K.-S., et al. 2011, *ApJ*, 731, L17  
Collins, J. A., Shull, J. M., & Giroux, M. L. 2009, *ApJ*, 705, 962  
Cooper, J. L., et al. 2008, *ApJ*, 674, 157  
Crocker, R. M. 2012, *MNRAS*, 423, 3512  
Crocker, R. M., & Aharonian, F. 2011, *PhRvL*, 106, 101102  
Dijkstra, M. & Kramer, R. 2012, *MNRAS*, 424, 1672  
Dobler, G., & Finkbeiner, D. P. 2008, *ApJ*, 680, 1222  
Dobler, G., et al. 2010, *ApJ*, 717, 825  
Finkbeiner, D. P. 2004, *ApJ*, 614, 186  
Fox, A. J., et al. 2014, *ApJ*, 787, 147  
Green, J. C., et al. 2012, *ApJ*, 744, 60  
Guo, F., & Mathews, W. G. 2012, *ApJ*, 756, 181  
Heckman, T. M. 2002, *ASPC*, 254, 292  
Kataoka, J., Tahara, N., Totani, T., et al. 2013, *ApJ*, 779, 57  
Keeney, B. A., et al. 2006, *ApJ*, 646, 951  
Lacki, B. C. 2014, *MNRAS*, 444, L39  
Lehner, N., et al. 2012, *MNRAS*, 424, 2896  
Lockman, F. J. 1984, *ApJ*, 283, 90  
McClure-Griffiths, N. M., et al. 2013, *ApJ*, 770, L4 (MG13)  
McCourt, M., et al. 2014, *MNRAS*, submitted (arXiv:1409.6719)  
Mou, G., Yuan, F., Bu, D., Sun, M., & Su, M. 2014, *ApJ*, 790, 109  
Murray, N., et al. 2005, *ApJ*, 618, 569  
Ohyama, Y., et al. 2002, *PASJ*, 54, 891  
Putman, M. E., et al. 2012, *ARA&A*, 50, 491  
Reid, M. J., et al. 2009, *ApJ*, 700, 137  
Ryans, R. S. I. et al. 1997, *ApJ*, 490, 267  
Savage, B. D., & Massa, D. 1987, *ApJ*, 314, 380  
Savage, B. D., et al. 1990, *ApJ*, 355, 114  
Savage, B. D., et al. 2001, *ApJS*, 136, 631  
Sembach, K. R., et al. 1991, *ApJ*, 372, 81  
Shoppell, P. L., & Bland-Hawthorn, J. 1998, *ApJ*, 493, 129  
Shull, J. M., et al. 2009, 699, 754  
Snowden, S., Egger, R., Freyberg, M., et al. 1997, *ApJ*, 485, 125  
Su, M., Slatyer, T. R., & Finkbeiner, D. P. 2010, *ApJ*, 724, 1044  
Veilleux, S., & Rupke, D. 2002, *ApJ*, 565, L63  
Veilleux, S., et al. 2005, *ARA&A*, 43, 769  
Wakker, B. P., et al. 2012, *ApJ*, 749, 157  
Yang, H.-Y. K., et al. 2012, *ApJ*, 761, 185  
Zech, W. F., et al. 2008, *ApJ*, 679, 460  
Zubovas, K., et al. 2011, *MNRAS*, 415, L21